Carrier Phase Ionospheric Gradient Ground Monitor for GBAS with Experimental Validation

SAMER KHANAFSEH
Illinois Institute of Technology

SAM PULLEN
Stanford University

JOHN WARBURTON
William J. Hughes FAA Technical Center

ABSTRACT: *This paper describes a Ground Based Augmentation System (GBAS) ground-based monitor capable of instantly detecting anomalous ionospheric gradients. The monitor utilizes differential carrier phase measurements across multiple reference station baselines as the basis for detection. Performance analysis shows that the monitor is highly sensitive to the quality of the carrier phase measurements. Therefore, data collected from a GBAS prototype ground facility is used to quantify the measurement quality and validate the concept monitor. Copyright © 2012 Institute of Navigation.*

INTRODUCTION

The Federal Aviation Administration (FAA) has sponsored two programs to augment GPS for civil aviation applications: the Wide Area Augmentation System (WAAS), which is referred to internationally as a Space Based Augmentation System (SBAS), and the Local Area Augmentation System (LAAS), commonly referred to as a Ground Based Augmentation System (GBAS). GBAS is a safety-critical system that is intended to support all close-proximity flight procedures including landing, departure, and surface operations at an airport. The main advantages of GBAS, relative to the existing Instrument Landing System (ILS), are its ability to support multiple types of approaches and its ability to support operations at several runways simultaneously with a single Ground Facility (GF). Because of its versatility, GBAS is envisioned to replace ILS, which is currently being used for final approach and landing phases of flight. Each GF will include multiple, spatially separated GPS receivers utilizing Low Multipath Antennas (LMAs). The primary reasons for the use of multiple reference receivers and antennas at the GF are to provide a means for detection and isolation of a failed receiver and also to allow for a net reduction in ranging error by averaging measurements for a given satellite.

However, a generally unrecognized benefit of such antenna separation is that differential carrier phase measurements across the baselines can be used to detect and isolate certain signal-in-space (SIS) failures and anomalies that are hazardous to GBAS. Examples of such SIS failures are ephemeris anomalies and ionospheric fronts. In this work, we will focus on ionospheric front detection and mitigation.

The ionosphere is a region of ionized gases that extend from 50 km to about 1000 km above Earth's surface. When the GPS radio signal travels through this region a change occurs in its speed and direction (usually referred to as refraction), which has a direct impact on the calculation of user-to-satellite range. Because of the dispersive nature of the ionosphere, GPS code and carrier measurements are affected differently: the ionosphere delays the code phase signal and advances the carrier phase signal by the same amount. This phenomenon is commonly referred to as code-carrier divergence. The state of the ionosphere changes over a given day and night and is also highly influenced by solar activity, such as solar storms and geomagnetic disturbances. Nominal spatial and temporal variations in the ionospheric delays are accounted for in GBAS and do not pose a threat. However, unusual behavior during ionospheric storms may result in large spatial gradients of up to 400 mm/km in slant ionospheric delay (meaning 400 mm slant error in the

measurement per one kilometer of distance between two antennas), which are referred to as ionospheric fronts [1–4]. Such fronts have been observed in 2000 and 2003 and are detailed in [1–4]. For an approaching aircraft using GBAS, gradients this large could cause vertical position errors of up to 20 m [4]. More details about the hazardous impact of sharp ionospheric fronts on GBAS navigation are discussed in [4].

At the GF, existing monitors use code-carrier divergence to help detect ionospheric fronts [5]. Another type of monitor which uses triple difference carrier phase measurements for fault detection is described in [6]. The major disadvantage of these monitors is that they require a time history of measurements and cannot detect ionospheric fronts present at satellite acquisition (i.e., the first time the satellite is used). In other words, if a newly acquired satellite is affected by an ionospheric front, such a monitor will not be able to detect it. Subsequent monitor performance may also be affected due to the presence of the front at the commencement of monitoring. In this case, it is necessary for ground-based fault detection to rely on instantaneous GF measurements directly.

First, this paper will tackle the issue of instantaneously detecting ionospheric fronts. We will begin by considering a monitor capable of instantaneously detecting ionospheric fronts using double difference carrier phase measurements. The performance of this monitor is quantified as a function of ionospheric front gradient, baseline length, and carrier phase measurement quality. Due to the high sensitivity of monitor performance on carrier phase measurement quality, data validation is presented and discussed. Finally, improvements to the monitor performance via calibration of the LMA antenna phase center variation are discussed.

IONOSPHERIC FRONT MONITOR CONCEPT

The concept explained herein is based on the work in [7]. A very effective method toward detecting ionospheric fronts instantaneously is to use double difference carrier phase measurements between the known LMA baselines to directly observe the effect of the ionospheric anomalies. This method utilizes differences in baseline lengths to cover different ionospheric front gradient magnitudes. Under nominal conditions (fault free), a simplified version of the single difference (two reference station antennas constructing a baseline $\mathbf{x}_b$) carrier phase measurement can be written as,

$$\Delta\phi = \mathbf{e}^T \mathbf{x}_b + \Delta\tau + \lambda\,\Delta n + \Delta b_I + \varepsilon_{\Delta\phi} \qquad (1)$$

where,

$\Delta\phi$ the single difference carrier phase measurement vector

$\mathbf{e}$ user-satellite unit line of sight vector

$\mathbf{x}_b$ baseline vector between the two antennas,

$\Delta\tau$ differential receiver clock bias

λ carrier phase wavelength

Δn single difference ambiguity

Δb_I differential ionospheric error between the antennas (baseline), and

$\varepsilon_{\Delta\phi}$ the single difference carrier phase measurement noise.

Under nominal ionospheric conditions, if the baseline length is relatively short (less than a kilometer), Δb_I will be on the order of millimeters and usually can be neglected. If an ionospheric front exists, the ionospheric front gradient will be significant and might cause an erroneous position estimate due to substantial Δb_I. For simplicity, the ionospheric front is modeled as a slant gradient α connecting two zones. Note that since α is expressed as a slant gradient, there is no need to apply an obliquity factor to the measurements. Furthermore, it is assumed that the baseline between the antennas in the GBAS GF is aligned with the runway for the landing approach. Therefore, the ionospheric error is the product of the baseline length with the effective ionospheric slant gradient. In this case, Equation (1) becomes:

$$\Delta\phi = \mathbf{e}^T \mathbf{x}_b + \Delta\tau + \lambda\,\Delta n + \alpha\,\|\mathbf{x}_b\| + \boldsymbol{\varepsilon}_{\Delta\phi} \qquad (2)$$

Pullen, et al. [4] found that in CONUS, α could be as large as 425 mm/km. They also stated that much higher values are expected in more active regions near the equator. In order to be conservative, it is assumed that values of up to 2000 mm/km can occur in the conducted analysis later in this paper. For the case of single-frequency GBAS Approach Service Type D (GAST-D) CAT III, the current Standards and Recommended Practices (SARPs) requirement limits the responsibility of the ground system monitor to detection of gradients above 300 mm/km [8]. The reason for this is that an extensive analysis of the airborne monitoring system provided in GAST-D showed that only fronts which are larger than 300 mm/km, and are undetected by the GF monitors, are potentially hazardous [8].

Assuming that both receivers have clock steering turned on, differencing the carrier phase measurement of another satellite (reference satellite) from Equation (2) (known as double difference measurement) eliminates the receiver clock bias and retains the gradient as shown in Equation (3).

$$\Delta^2\phi = \Delta\mathbf{e}^T \mathbf{x}_b + \lambda\,\Delta^2 n + \alpha\,\|\mathbf{x}_b\| - \alpha^*\,\|\mathbf{x}_b\| + \boldsymbol{\varepsilon}_{\Delta^2\phi} \quad (3)$$

where α^* is the ionospheric slant gradient for the reference satellite. The front characteristics in [9] dictate that only a small portion of the sky will be affected by a given front, ensuring that a fault free

satellite exists and can indeed be used. Therefore, the term $\alpha^* \|\mathbf{x}_b\|$ can be neglected from (3) by computing the double difference using a satellite that has already been validated as fault-free.

Since the line-of-sight to each satellite is computed from the ephemeris and the baseline vector between the GF antennas is known, the first term on the right hand side of Equation 3 can be removed from the measurements:

$$\Delta^2\phi - \Delta\mathbf{e}^T\mathbf{x}_b = \lambda\Delta^2 n + \alpha \ \|\mathbf{x}_b\| + \boldsymbol{\varepsilon}_{\Delta^2\phi} \qquad (4)$$

Separating the ionospheric front error from the ambiguities in Equation (4) is quite challenging. However, it is known that the ambiguities can only take on integer values. Therefore, if the measurement noise is ignored, a necessary condition for the detection of an ionospheric front is that the value of $\alpha \|\mathbf{x}_b\|$ is not equal to an integer multiple of λ. This fact forms the basis of the instantaneous ionospheric front detection monitor.

Now let us consider the case with measurement noise. The carrier phase measurement noise is assumed to be bounded by a Gaussian distribution with zero mean and a standard deviation σ_ϕ. Therefore, the noise term in Equation (4) will be normally distributed with zero mean and a standard deviation of $\sigma_{\Delta^2\phi} = 2\sigma_\phi$. Based on the concept described earlier, the test statistic s is defined as

$$s = \Delta^2\phi - \Delta\mathbf{e}^T\mathbf{x}_b - \lambda\,\text{round}\left(\frac{\Delta^2\phi - \Delta\mathbf{e}^T\mathbf{x}_b}{\lambda}\right) \quad (5)$$

Under fault free conditions, this test statistic has a zero mean and a standard deviation of $\sigma_{\Delta^2\phi}$. Given an acceptable false alarm probability under fault free conditions, P_{ffd}, a detection threshold can be defined as:

$$T = k_{ffd} \ \sigma_{\Delta^2\phi} \qquad (6)$$

where k_{ffd} is the false alarm multiplier computed from the inverse of the standard normal cumulative distribution function (Φ) as

$$k_{ffd} = -\Phi^{-1}\left(\frac{P_{ffd}}{2}\right) = -\sqrt{2} \ \text{erf}^{-1}\left(P_{ffd} - 1\right) \qquad (7)$$

The probability of missed detection P_{md} of this monitor must also comply with the integrity risk requirement. Therefore, given that there is a fault (ionospheric front), the probability that the test statistic will be less than the threshold must meet the required P_{md}. As shown in Figure 1, a minimum detectable error (MDE) can then be defined using the threshold and P_{md}. Using a similar approach to Equations (6) and (7), the MDE becomes

$$MDE = T + k_{md}\sigma_{\Delta^2\phi} = \left(k_{ffd} + k_{md}\right)\sigma_{\Delta^2\phi}, \qquad (8)$$

where k_{md} is the missed detection multiplier and is computed as

$$k_{md} = -\Phi^{-1}(P_{md}) = -\sqrt{2} \ \text{erf}^{-1}(2P_{md} - 1). \qquad (9)$$

Due to the existence of a nearby integer with its own MDE buffers, there will also be a maximum detectable error. This case is better illustrated in Figure 2. The origin point (corresponding to point 0) represents the integer value of λ round$[(\Delta^2\phi - \Delta\mathbf{e}^T \mathbf{x}_b)/\lambda]$. The minimum detectable $\alpha\|\mathbf{x}_b\|$ about integer 0 is given by $(k_{ffd} \ \sigma_{\Delta^2\phi} + k_{md} \ \sigma_{\Delta^2\phi})$. Gradients larger than this value are detectable while satisfying the required availability and integrity requirement allocations. However, there is also an upper bound to the detectable gradient because of the presence of the adjacent integer and the undetectable region around it. In other words, if $\alpha \ |\mathbf{x}_b|$ is significant, it might fall close to another integer where it cannot be detected with the required probability. This illustration can be expressed in a mathematical form that defines the undetected ionospheric slant gradient band as

$$\frac{\lambda n - \left(k_{ffd} + k_{md}\right)\sigma_{\Delta^2\phi}}{\|\mathbf{x}_b\|} < \alpha < \frac{\lambda n + \left(k_{ffd} + k_{md}\right)\sigma_{\Delta^2\phi}}{\|\mathbf{x}_b\|} \quad (10)$$

where n here is an arbitrary integer number.

The effectiveness of this monitor is fundamentally based on the widths of the detection bands, which in turn are directly related to the baseline
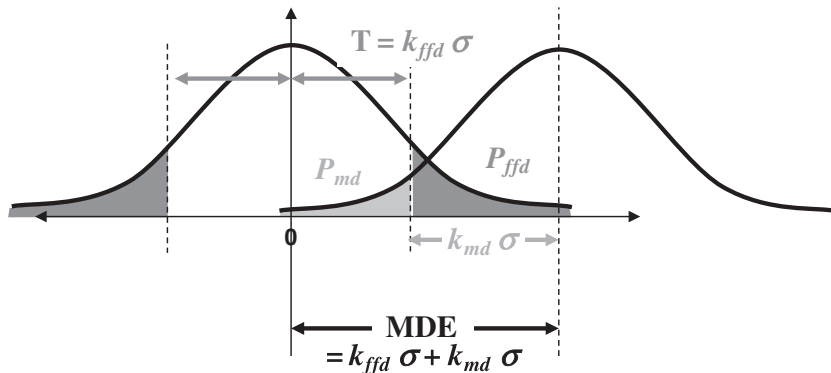

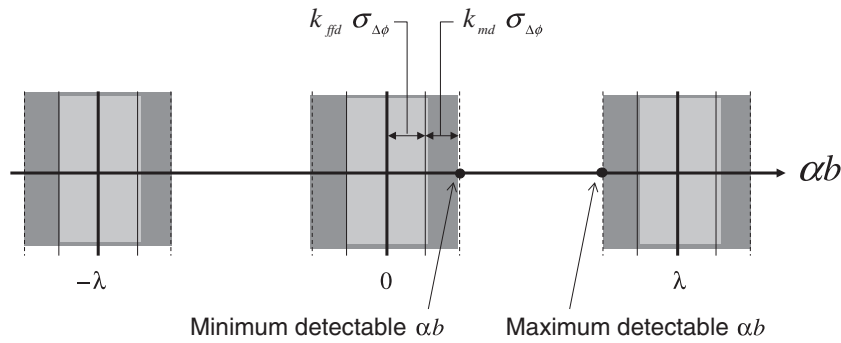Fig. 1–Detection principles used to define the threshold and MDE

Fig. 2–Illustration of the undetectable lanes around each integer

lengths, k_{ffd}, k_{md}, and the quality (standard deviation) of the differential carrier phase measurement error. As an example, suppose that P_{md} and P_{ffd} are 10^{-4}. This value for P_{ffd} was chosen as a conservative number given an availability requirement of 99.9%. Given that the GBAS integrity risk requirement is 10^{-9}, setting P_{md} equal to 10^{-4} is based on a prior probability of an ionospheric front occurring. Using these values in (7) and (9), we conclude that k_{md} and k_{ffd} are 3.7 and 3.9, respectively. Assuming that $\sigma_{\Delta^2\phi}$ is 3 mm, it is possible to plot regions of non-detectable slant gradient as a function of baseline length. These regions are shown as shaded lanes in Figure 3. Other values of $\sigma_{\Delta^2\phi}$ have also been used to generate similar plots in Figures 4–6.

Figure 3 shows bands of detectable ionospheric fronts (white spaces) and bands of undetectable fronts (shaded). These shaded bands are due to the buffer zones around the nearby integers illustrated in Figure 2. Therefore, as the carrier phase measurements become more noisy (larger $\sigma_{\Delta^2\phi}$) these shaded lanes will also get thicker to the point where no detectable space is left. In contrast, as the carrier phase measurement quality improves (smaller $\sigma_{\Delta^2\phi}$) the undetectable shaded lanes get thinner leaving wider detection spaces. This in turn suggests that larger gradients can be detected using several baseline options and siting flexibility. For example, in Figure 3, a 100 m baseline (which is currently being used at the LGF) is sufficient to detect slant gradients from 250 – 1600 mm/km. If this baseline is combined with another of 175 m, the detection range increases to 140 – 2000 mm/km.

If $\sigma_{\Delta^2\phi}$ increases to 6 mm (Figure 4), the range of detectable slant gradients using a 100 m baseline decreases to 470 – 1450 mm/km. By adding another 300 m baseline, the monitor will be able to detect gradients in the range of 170 – 1750 mm/km. Figure 5
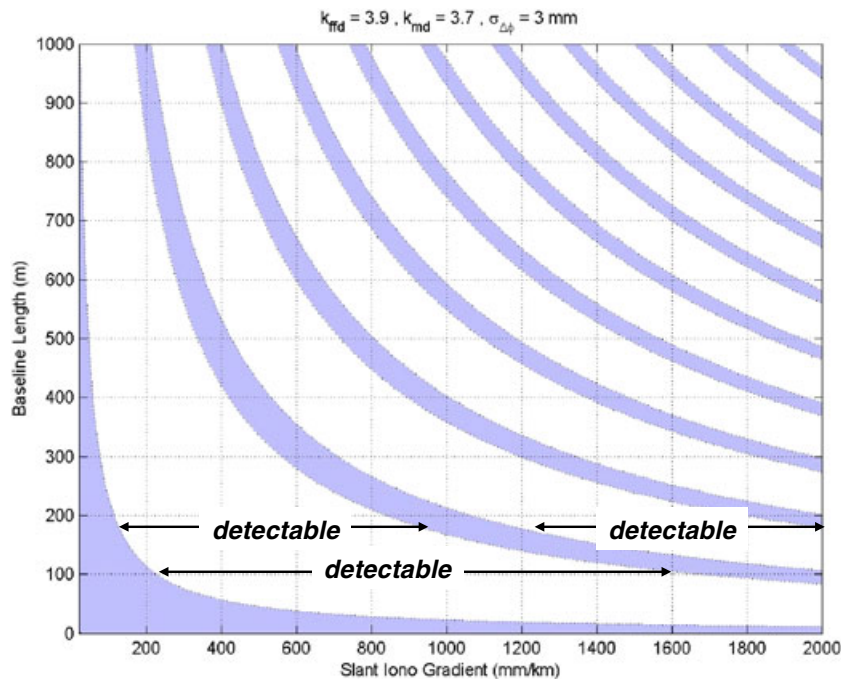

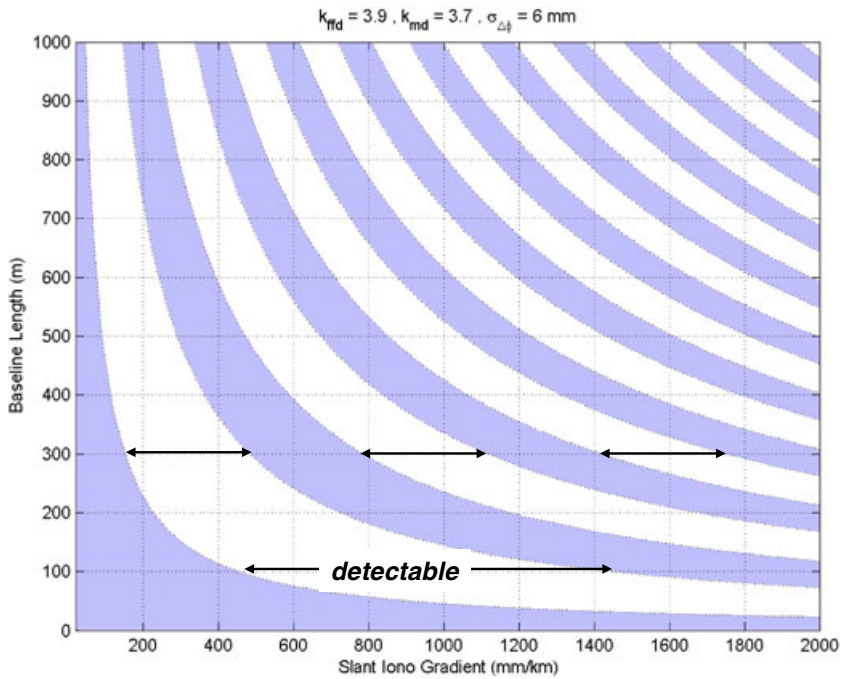Fig. 3–Detection performance for the instantaneous monitor with $\sigma_{\Delta^2\phi}$ = 3 mm

Fig. 4–Detection performance for the instantaneous monitor with $\sigma_{\Delta^2\phi} = 6\,\text{mm}$
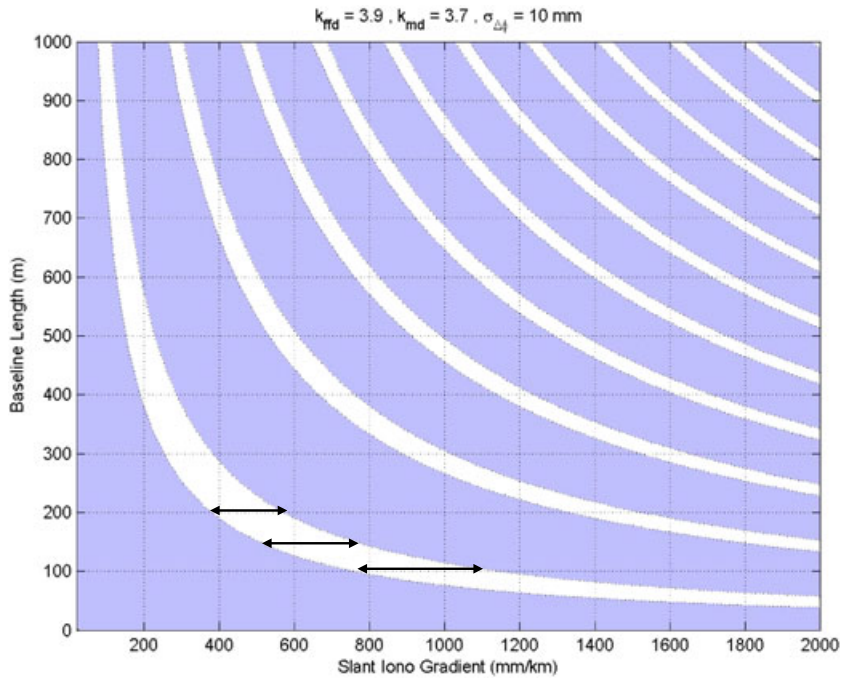

Fig. 5–Detection performance for the instantaneous monitor with $\sigma_{\Delta^2\phi} = 10\,\text{mm}$

shows the case when $\sigma_{\Delta^2\phi}$ is 10 mm. In this case, the undetectable lanes get even thicker leaving small detection ranges. Therefore, multiple carefully chosen baselines are necessary even to detect an ionospheric gradient ranging from 190 – 1100 mm/km. If the measurement quality becomes so poor that $\sigma_{\Delta^2\phi}$ is 12 mm or more, the monitor is no longer feasible for instantaneous ionospheric front detection. This situation is

depicted in Figure 6, where no detection space is left when the measurement noise reaches 13 mm (1σ).

Even though the results shown in Figures 3–6 were obtained for specific values of P_{ffd} and P_{md}, they can be generalized to other values of P_{ffd} and P_{md} by appropriately modifying the value of $\sigma_{\Delta^2\phi}$ for each plot. For example, Figure 3 (which was generated using $\sigma_{\Delta^2\phi} = 3\,\text{mm}$) is in fact for a case where
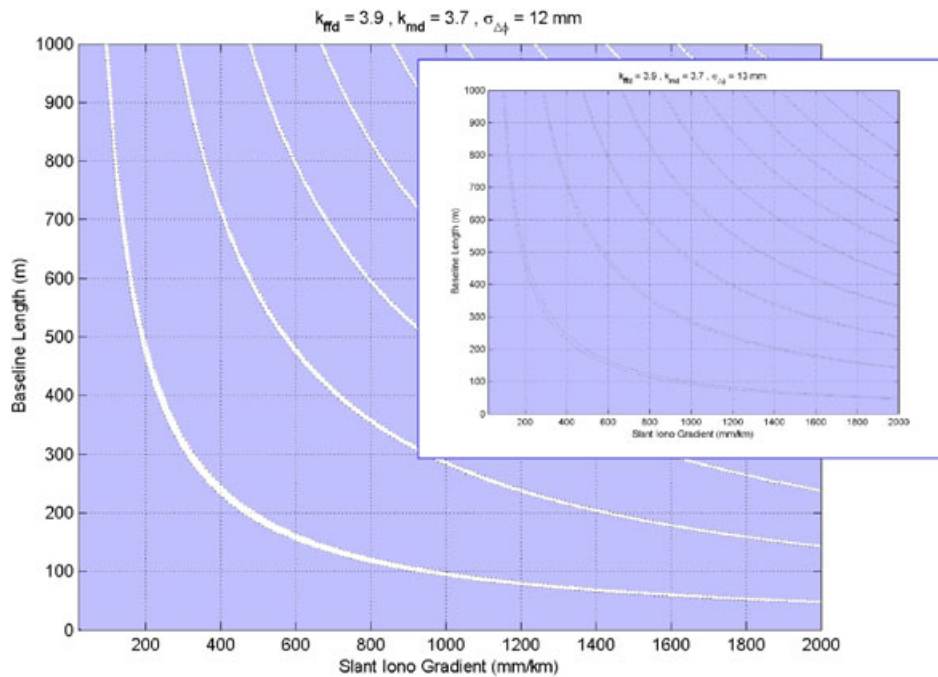
$(k_{ffd} + k_{md})\sigma_{\Delta^2\phi}$ = 22.8 mm. Therefore, if different values for k_{ffd} and k_{md} are required, the figure will correspond to a value of $\sigma_{\Delta^2\phi}$ that is equal to 22.8/$(k_{ffd} + k_{md})$ mm. Figures 4–6 can be reinterpreted similarly.

In summary, the monitor feasibility is sensitive to the quality of the carrier phase measurements. The uses envisioned here for the GBAS LMAs pose a new challenge because such precision for carrier phase measurements is not required for the nominal fault-free GBAS functionality and was not a specific requirement in the design of these antennas. The exceptional theoretical thermal noise and multipath performance of the LMA suggests that such carrier phase precision should be achievable in principle, but the behavior of the antennas in detail at the millimeter level must be experimentally analyzed. Of particular importance in this regard are the potential variations in phase patterns between antennas, which will be discussed next.

EXPERIMENTAL VALIDATION

To examine the performance of the LMA, measurements were collected from four LMA antennas at the LAAS Test Prototype (LTP) facility at the William J. Hughes FAA Technical Center in Atlantic City, New Jersey. The LMA is an array antenna that covers elevation angles of 5–90 deg; it is resistant to terrestrial interference sources and meets the signal-to-noise ratio and multipath rejection requirements at low elevations. Although the antenna phase center variations are bounded by a few centimeters, in the previous section we showed that the measurement accuracy required by the instantaneous ionospheric front monitor must be within millimeters. In this paper, results will be shown for an example antenna pair (the first two antennas).

Figure 7 shows an example of the double difference carrier phase residual for one satellite (PRN 31). This residual is computed as
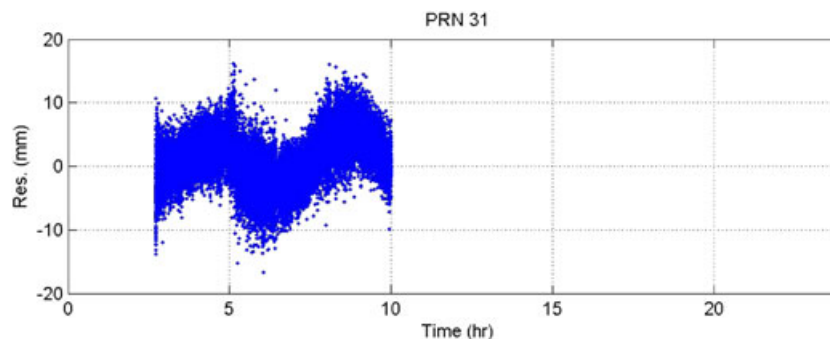

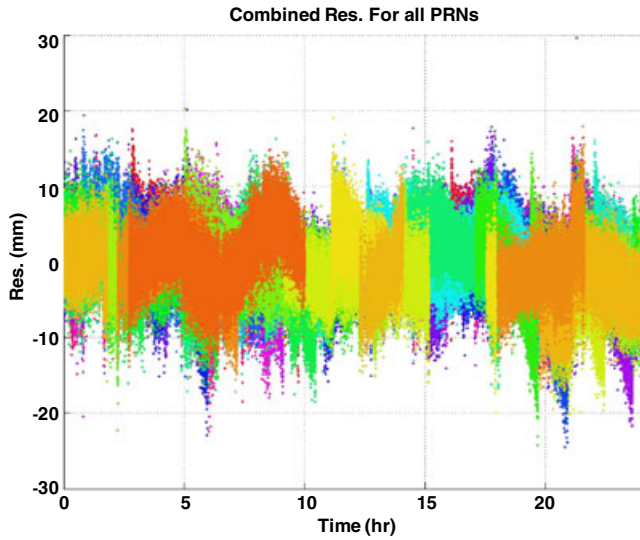Fig. 7–Double difference carrier phase residual for PRN 31

Fig. 8–Double difference carrier phase residual for all visible satellites

Fig. 9–Folded CDF for the residuals in Figure 8 with three over-bounding Gaussian curves.

$$r = \Delta^2\phi - \Delta\mathbf{e}^T\mathbf{x}_b - \lambda\,\mathrm{round}\left(\frac{\Delta^2\phi - \Delta\mathbf{e}^T\mathbf{x}_b}{\lambda}\right) \quad (11)$$

As shown in Figure 7, non-random residual errors are larger and occur at lower frequencies than those that can be caused by multipath and thermal noise variations. This behavior is not unique to this particular satellite. Figure 8 shows a composite of all visible satellites over a 24 h period in which several satellites display similar wavy patterns in their residuals. Furthermore, the residual wavy pattern shows day-to-day repeatability indicating that the source of the effect is a systematic difference in the phase patterns between antennas. This pattern cannot be ignored because of its effect on increasing the standard deviation of the double difference residual.

Since this monitor will be used in high integrity applications, simply computing an estimate of the standard deviation ($\sigma_{\Delta^2\phi}$) of the residual errors is not enough to ensure integrity. Instead, the tails of the distribution must be appropriately overbounded by a Gaussian distribution with a standard deviation that is inflated relative to this estimated value. A common method of constructing an overbound is to use the folded cumulative distribution function (CDF). The folded CDF is a CDF where one minus the cumulative probability is plotted on a y-axis (in log scale) for cumulative probabilities greater than one half. In Figure 9, the CDF for all satellite residuals is shown. Alongside the residual folded CDF is a theoretical over-bounding Gaussian folded CDF with a zero mean and various sigma values (dashed curves). The figure shows that the residual CDF cannot be overbounded by a standard deviation of up to 6 mm, which is not a promising result for the front monitor.
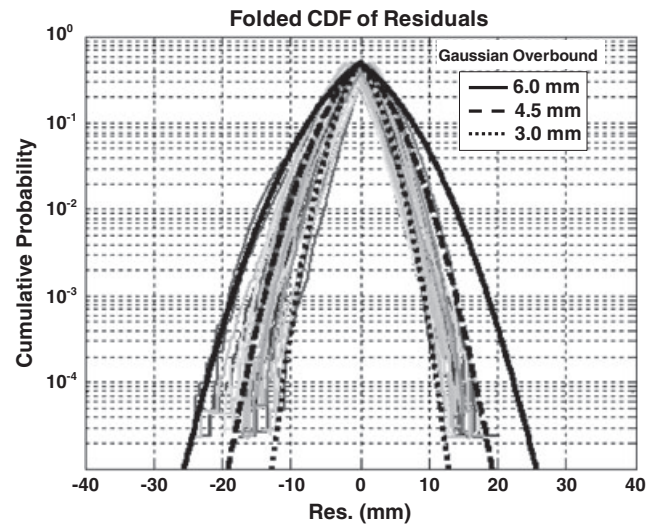
Removal of the undesired systematic effects is necessary to achieve the levels of residual carrier phase error needed for the monitor applications under consideration. In this regard, the differential phase pattern behavior was captured as a function of satellite azimuth and elevation by fitting a full day's worth of LTP satellite data to a spherical harmonic model. In previous work [6], similar models have been used to calibrate the Integrated Multipath Limiting Antennas (IMLA).

Spherical Harmonics Model

A spherical harmonics function of order k is composed of a Legendre trigonometric polynomial series of order n and degree m (Equation (12)). This function is able to capture the observed variation as a function of azimuth and elevation.

$$U(\theta,\psi) = \sum_{n=0}^{k} J_n P_{n0}(\cos\theta) + \sum_{n=1}^{k}\sum_{m=1}^{n}[C_{nm}\cos(m\psi) \quad (12)$$
$$+ S_{nm}\sin(m\psi)]P_{nm}(\cos\theta)$$

where,

J_n, C_{nm} and S_{nm} spherical harmonic coefficients
θ zenith angle
ψ azimuth angle, and
P_{nm} Legendre polynomial of order n, degree m, and is defined as

$$P_{nm}(\cos\theta) = 2^{-n}(\sin\theta)^m\sum_{q=0}^{l}(-1)^q$$
$$\times\frac{(2n-2q)!}{q!(n-q)!(n-m-2q)!}(\cos\theta)^{n-m-2q}$$

where $l = \mathrm{floor}\left\{\frac{n-m}{2}\right\}$.

$$U_{ab}(\theta^i, \psi^i) - U_{ab}(\theta^j, \psi^j) = \sum_{n=0}^{k} \Delta J_{nm} \left[P_{n\,0}(\cos\theta^i) - P_{n\,0}(\cos\theta^j) \right]$$
$$+ \sum_{n=1}^{k} \sum_{m=1}^{n} \Delta C_{nm} \left(\cos(m\psi^i) - \cos(m\psi^j) \right) \left[P_{nm}(\cos\theta^i) - P_{nm}(\cos\theta^j) \right] \qquad (14)$$
$$+ \sum_{n=1}^{k} \sum_{m=1}^{n} \Delta S_{nm} \left(\sin(m\psi^i) - \sin(m\psi^j) \right) \left[P_{nm}(\cos\theta^i) - P_{nm}(\cos\theta^j) \right]$$

The model used to calibrate the antennas uses the double difference carrier phase residual. Therefore, the spherical harmonics function in Equation (12) must be written in terms of the double difference quantities: azimuth and elevation angles of both satellites i and j and the two antennas a and b.

$$r = U_{ab}(\theta^i, \psi^i) - U_{ab}(\theta^j, \psi^j) + v_{\Delta^2\phi} \qquad (13)$$

where U_{ab} is written in terms of baseline antennas calibration coefficients ΔJ_{nm}, ΔC_{nm}, and ΔS_{nm} as,

Since Equation (14) is linear in respect to the calibration coefficients, it can be written in a vector form as

$$\mathbf{r} = \mathbf{P}_\Delta \mathbf{c} + \mathbf{v}_{\Delta^2\varphi} \qquad (14)$$

where $\mathbf{r}$ is the residual vector, $\mathbf{P}_\Delta$ is a matrix containing the Legendre polynomials P and $\mathbf{c}$ is a vector that contains the coefficients ΔJ_{nm}, ΔC_{nm}, and ΔS_{nm}.

The spherical harmonics coefficient vector $\mathbf{c}$ in Equation (14) can be estimated using a Kalman filter for all satellites in view using a 24 h data set. The

results of this filtering process are shown in Figure 10. The processed satellite passes (azimuth and elevation angles) are shown in the sky plot in Figure 10-a. In the calibration process, an 8th order model ($k = 8$) was used because it was concluded in [6] that an 8th order model is sufficient to reduce the wave amplitude. Using this estimated ΔK_{nm}, a calibration map for all azimuth and elevation angles is generated and the correction magnitude is represented in the contour plot in Figure 10-b. This calibration is valid for the specific baseline under consideration and a different calibration map must be created for other baselines. Since no data was available in the northern section of the sky map (as illustrated by the sky plot in Figure 10-a), calibration at this area is not representative and was not included in the contour plot of Figure 10-b. Notice that the sky maps are not symmetric, which again suggests that the cause is individual phase center variations of these antennas.

The corrected residuals using the spherical harmonics model are shown in Figure 11. The experimental results show that using a one-time calibration, the systematic wave patterns have been removed. Also, Figure 12 shows the CDF of the corrected residuals
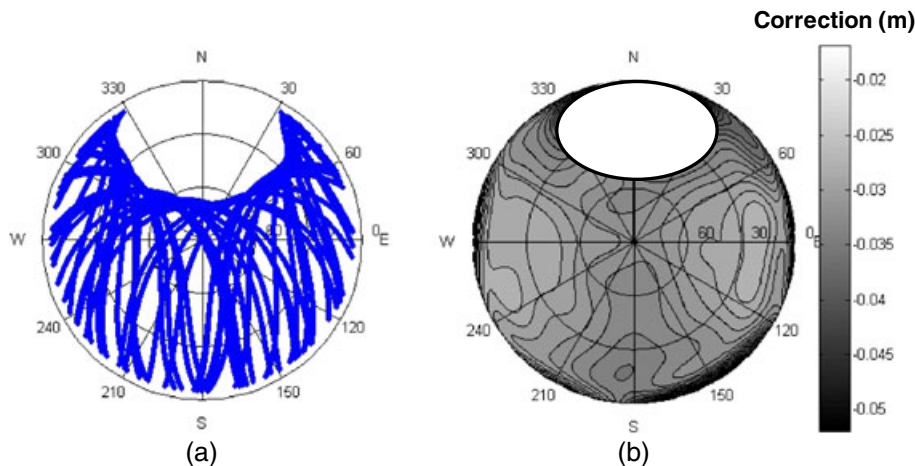

Correction (m)

(a)   (b)

Fig. 10–a- Azimuth-elevation sky plot showing the satellite passes that are used in estimating the spherical harmonics coefficients, b- Contour plot showing the magnitude of the resulting spherical harmonics corrections that are used to calibrate the antennas.
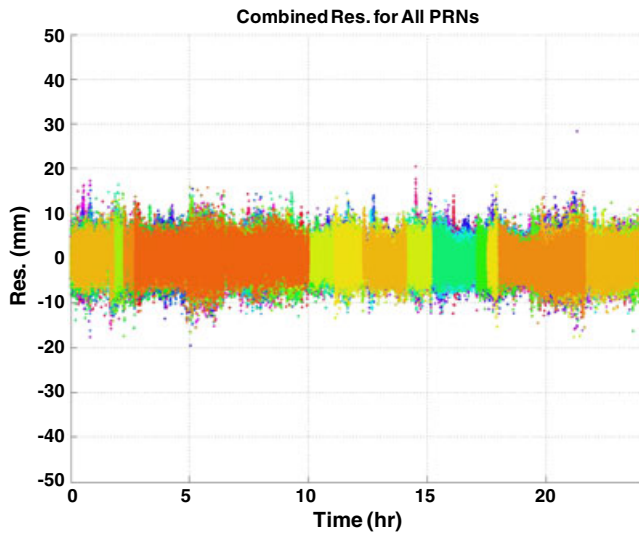
Fig. 11–Calibrated double difference carrier phase residual for all visible satellites
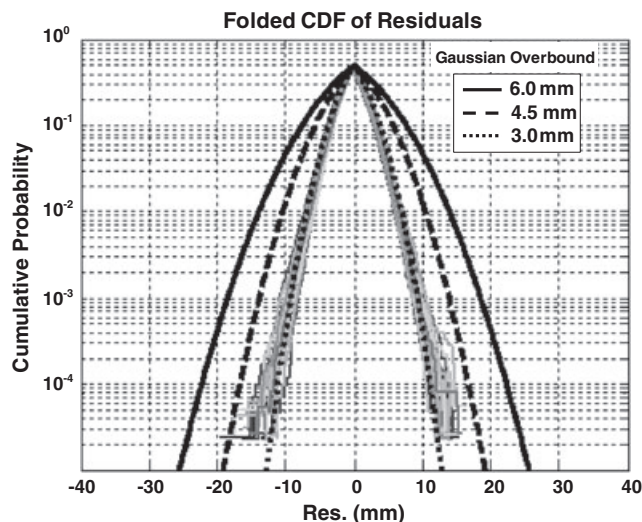

Fig. 12–Folded CDF for the calibrated residuals in Figure 11 with three overbounding Gaussian curves.

with three overbounding Gaussian CDFs. The figure shows that if a standard deviation of 3 mm is used, the tails are not overbounded. The standard deviation must be inflated to 4.5 mm to overbound the residual CDF out to a probability of 10^{-4}. It should be noted that the remaining points that are not overbounded by this distribution were caused by outliers that were observed in the data. In order to be conservative, a standard deviation of 6 mm is used as an overbound. This value is also consistent with the residual results for all baselines. As a result, this monitor is feasible for detecting ionospheric slant gradients as shown in Figure 4. Using that figure, different baseline combinations can be chosen to cover the desired range of slant gradients to be detected.

The calibration map and the estimated coefficients are antenna and site dependent. If this calibration is performed using different antennas or is performed at any other airport or facility, new coefficients must be estimated. Nevertheless, in principle, this type of calibration should be valid for all times given that the antennas and siting locations have not changed. The source of outliers that are observed in Figures 8 and 11 and high tail activity (Figures 9 and 12) in the LTP data will also be investigated. Data from other installations at busy airports will also be considered. Furthermore, the monitor concept will be generalized to detect ionospheric front anomalies at all times (instead of only at the time of acquisition) and to potentially extend its capabilities to detect other anomalies like ephemeris failures.

CONCLUSIONS

This paper describes in detail an instantaneous monitor for detecting ionospheric front anomalies using double differential carrier phase measurements. The monitor utilized GBAS ground antenna baselines for detection. It was shown that certain combinations of baseline lengths can extend the range of detectable ionospheric slant gradients. However, in order for such a monitor to be feasible, the carrier phase measurement noise must be less than 10 mm. In order to validate the feasibility of this monitor, carrier phase performance of typical GBAS LMA antennas has been analyzed. An assessment of differential phase pattern variations with respect to azimuth and elevation has been presented. This paper defines the mathematical model developed for differential phase variation, explains its use in precise antenna calibration, and demonstrates that the resulting LMA double difference carrier phase errors can be overbounded by a standard deviation of 6 mm.

REFERENCES

1. Datta-Barua, S., Walter, T., Pullen, S., Luo, M., Blanch, J., and Enge, P., "Using WAAS Ionospheric Data to Estimate LAAS Short Baseline Gradients". *Proceedings of the 2002 National Technical Meeting of The Institute of Navigation*, San Diego, CA, January 2002, pp. 523–530.
2. Datta-Barua, S., Walter, T., Pullen, S., and Enge, P., "Modeling the 20 November 2003 Ionosphere Storm with GRACE." *Proceedings of the 20th International Technical Meeting of the Satellite Division of The Institute of Navigation (ION GNSS 2007)*, Fort Worth, TX, September 2007, pp. 2840–2848.
3. Ene, A., Qiu, D., Luo, M., Pullen, S., and Enge, P., "A Comprehensive Ionosphere Storm Data Analysis Method to Support LAAS Threat Model Development." *Proceedings of the 2005 National Technical Meeting of The Institute of Navigation*, San Diego, CA, January 2005, pp. 110–130.
4. Pullen, S., Park, Y. S., and Enge, P., "Impact and mitigation of ionospheric anomalies on ground-based

augmentation of GNSS." *Radio Science*, Vol. 44, RS0A21, 2009. DOI: 10.1029/2008RS004084.

5. Simili, D. V., and Pervan, B., "Code-Carrier Divergence Monitoring for the GPS Local Area Augmentation System." *Proceedings of IEEE/ION PLANS 2006*, San Diego, CA, April 2006, pp. 483–493.

6. Gratton, L., Khanafseh, S., Pervan, B., Pullen, S., Warburton, J., and Hughes, W. J., "Experimental Observations and Integrity Monitor Applications of LAAS IMLA Carrier Phase Measurements." *Proceedings of the 17th International Technical Meeting of the Satellite Division of The Institute of Navigation (ION GNSS 2004)*, Long Beach, CA, September 2004, pp. 2259–2270.

7. Gratton, L., Chan, F., and Pervan, B., "Algorithms for Airborne Ionospheric Front Detection in LAAS Using Carrier Phase and INS Measurements." *Proceedings of the 2005 National Technical Meeting of The Institute of Navigation*, San Diego, CA, January 2005, pp. 131–139.

8. Murphy, T., Harris, M., Pullen, S., Pervan, B., Saito, S., Brenner, M., "Validation of Ionospheric Anomaly Mitigation for GAST D." ICAO NSP Working Group of the Whole (WGW) Meeting, Montreal, Canada, WGW/WP 14, May 17–28, 2010.

9. Luo, M., Pullen, S., Walter, T., and Enge, P., "Ionosphere Spatial Gradient Threat for LAAS: Mitigation and Tolerable Threat Space. *Proceedings of the 2004 National Technical Meeting of The Institute of Navigation*," San Diego, CA, January 2004, pp. 490–501.